Cesium Carbonate Functionalized Graphene Quantum Dots as Stable Electron-Selective Layer for Improvement of Inverted Polymer Solar Cells

Hong Bin Yang,[†] Yong Qiang Dong,[†] Xizu Wang,[‡] Si Yun Khoo,[†] and Bin Liu*,[†]

[†]School of Chemical and Biomedical Engineering, Nanyang Technological University, 62 Nanyang Drive, 637459, Singapore
[‡]Institute of Materials Research and Engineering, No. 3 Research Link, 117602, Singapore

Ⓢ Supporting Information

ABSTRACT: Solution processable inverted bulk heterojunction (BHJ) polymer solar cells (PSCs) are promising alternatives to conventional silicon solar cells because of their low cost roll-to-roll production and flexible device applications. In this work, we demonstrated that Cs_2CO_3 functionalized graphene quantum dots (GQDs−Cs_2CO_3) could be used as efficient electron-selective layers in inverted PSCs. Compared with Cs_2CO_3 buffered devices, the GQDs−Cs_2CO_3 buffered devices show 56% improvement in power conversion efficiency, as well as 200% enhancement in stability, due to the better electron-extraction, suppression of leakage current, and inhibition of Cs^+ ion diffusion at the buffer/polymer interface by GQDs−Cs_2CO_3. This work provides a thermal-annealing-free, solution-processable method for fabricating electron-selective layer in inverted PSCs, which should be beneficial for the future development of high performance all-solution-processed or roll-to-roll processed PSCs.

KEYWORDS: polymer solar cells, graphene, quantum dots, cesium carbonate, cathode buffer, stability
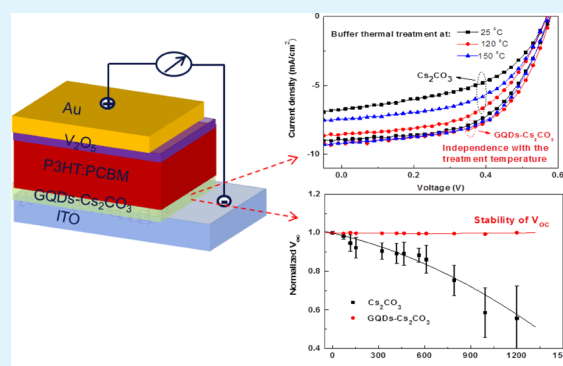
1. INTRODUCTION

Bulk heterojunction (BHJ) polymer solar cells (PSCs) have received notable scientific interest because of the potential for lowering the device fabrication costs by taking advantage of roll-to-roll solution processes and flexible device applications.[1−6] Among various forms of PSCs, inverted PSCs have received growing research attention because of their superior device stability and manufacturing compatibility.[7−9] In inverted PSCs, the interface between the two electrodes and the polymer active layer is crucial for the overall device performance and stability. The interface buffer should minimize the energy barriers for charge carrier extraction and in the meantime form a selective contact for electrons and block holes at cathode and vice versa at anode.[10−16] The state-of-the-art electron selection materials are solution-processed ZnO or TiO_2,[17−19] which can be spin-cast from respective precursors or presynthesized nanoparticles. A common phenomenon of PSCs incorporating ZnO or TiO_2 electron extraction buffer is the requirement of UV light soaking to achieve better performance; however, the improvement is not permanent.[19,20] On the other hand, Cs_2CO_3 was recently demonstrated as another promising cathode buffer due to the good electron injection and facile fabrication process.[21,22] However, the poor hole blocking ability of the Cs_2CO_3-modified ITO cathode significantly increases the recombination loss of electrons and holes at the cathode/polymer active layer interface and thus limits the device

performance. Moreover, the stability of PSCs buffered with Cs_2CO_3 is poor because of Cs^+ ion diffusion at the buffer/polymer interface, which damages the active polymer layer.[23,24]

Graphene quantum dots (GQDs), a new class of nanomaterials, offer unique photonic[25] and electronic properties,[26] which have been widely used in biological science,[27] photocatalysis,[28] light-emitting,[29,30] photoelectrochemical cells,[31] and photovoltaic devices.[32−34] In photovoltaics, GQDs were used as electron acceptors in organic/inorganic hybrid solar cells as well as sensitizers in QD-sensitized solar cells. However, the power conversion efficiencies of the respective solar cells are quite low. The surface of GQDs has many oxygen-rich functional groups; thus, the optical and electrical properties of GQDs can be tuned by modifying GQDs with functional groups, inorganic nanoparticles, and/or metal atoms.[35,36]

In this work, Cs_2CO_3 modified GQDs (GQDs−Cs_2CO_3) were investigated as the electron elective material in inverted PSCs. The effects of buffer surface morphology and work function of buffer layer modified ITO on the device performance were studied with PL, FTIR, XPS, and UPS. Our experimental results suggest that Cs_2CO_3 modified GQDs can work as excellent hole blocking buffer in inverted PSCs.
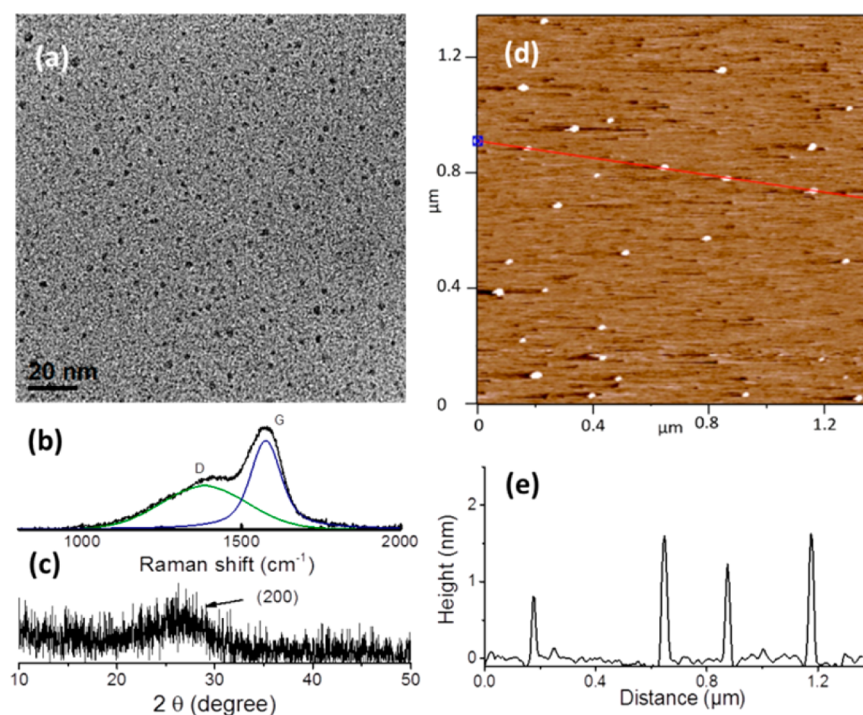
Figure 1. (a) TEM image, (b) Raman spectra, (c) XRD pattern, and (d) AFM image of the GQDs and (e) height profile along the line in (d).

The good performance of GQDs−Cs$_2$CO$_3$ buffer comes from the synergistic contributions from uniform buffer coating on ITO surface, good electron transfer, and excellent suppression of leakage current. Finally, the application of a solution-processed GQDs−Cs$_2$CO$_3$ buffer without any thermal treatment was demonstrated for improving the performance of inverted PSCs and process compatibility.

2. EXPERIMENTAL SECTION

2.1. Materials. All chemical reagents were purchased from Sigma-Aldrich and were used directly without further purification. Deionized water (resistivity over 18 MΩ cm) from a Millipore Q water purification system was used in all experiments.

2.2. Preparation of GQDs. GQDs were synthesized using a hydrothermal method developed in the literature.[25] In a typical synthesis, 2 g of citric acid monohydrate (9.5 mmol) and 1 g of L-cysteine (8.3 mmol) were dissolved in 5 mL of deionized water. The solution was evaporated until dry at 70 °C for 12 h. The resulting viscous syrup was heated in a Teflon-lined stainless steel autoclave at 200 °C for 3 h. Finally, the black syrup product was collected and dissolved in 2-ethoxyethanol.

2.3. GQDs and GQDs−Cs$_2$CO$_3$ Characterization. The morphologies of GQDs were examined with atomic force microscope (Nanoman, Veeco, Santa Barbara, CA) using tapping mode and transmission electron microscopy (HRTEM JEOL 2100). Fourier transform infrared spectra were obtained on a FTIR spectrophotometer (Thermo Nicolet 360). The crystal structures of the GQDs were characterized by X-ray diffraction (Bruker AXS, λ = 0.154 18 nm). Raman spectra were measured using a Renishaw 1000 microspectrometer (excitation wavelength of 514.5 nm). The chemical bonding information was examined with X-ray photoelectron spectroscopy (Kratos AXIS Ultra spectrometer) with a monochromatized Al Kα X-ray source (1486.71 eV). The optical properties were studied using a UV−vis spectrophotometer (UV-2450, Shimadzu). The photoluminesce (PL) and PL decay of Cs$_2$CO$_3$ modified GQDs were recorded using an LP920-KS instrument from Edinburgh Instruments, equipped with an iCCD camera from Andor and a photomultiplier tube. The PL lifetime was obtained by fitting PL decay curves with a monoexponential function. The work function of ITO

electrodes modified with different cathode buffers was examined using ultraviolet photoelectron spectroscopy with the helium line (21.2 eV).

2.4. Fabrication of Inverted PSCs. All devices with the structure of ITO/cathode buffer (Cs$_2$CO$_3$ or GQDs−Cs$_2$CO$_3$)/P3HT:PCBM/V$_2$O$_5$/Au were fabricated on precleaned ITO patterned glass substrates (sheet resistance of 15 Ω/□). The ITO substrates were ultrasonically cleaned in a mixed solution of water, ethanol, and 2-propanol (1:1:1 by volume) for 1 h, followed by oxygen plasma treatment for 10 min in vacuum. The cathode buffer was deposited on ITO substrates by spin-coating the GQDs (0−2 mg/mL)−Cs$_2$CO$_3$ (2 mg/mL) in 2-ethoxyethanol at 4000 rpm for 60 seconds. Then the buffer layer coated ITO substrates were baked on a hot plate in air for 20 min. Afterward, a poly(3-hexylthiophene-2,5-diyl) (P3HT, from Aldrich, regioregularity of ≥90.0%) and [6,6]phenyl-C61-butyric acid methyl ester (PCBM, from Nano-C (99.5% purity) blend in 1:1 weight ratio at a P3HT concentration of 20 mg/mL in chlorobenzene was spin-coated on the electron-selective layer/ITO surface at 700 rpm for 25 s (the active layer thickness was estimated to be ~180 nm) and dried in a covered Petri dish with a few drops of chlorobenzene for 20 min. Subsequently, the vanadium oxide (V$_2$O$_5$) anode buffer was coated on top of the polymer layer by spin-coating a vanadium precursor solution, vanadium oxytriisopropoxide in isopropanol (1:125 v/v), at 5000 rpm. The device fabrication was completed by thermal evaporation of a 50 nm gold film on top of the V$_2$O$_5$ buffer in vacuum ($P < 1.5 \times 10^{-5}$ Pa) as anode electrode. The illumination area of each device is defined by the area of gold electrode, which is ~7.06 mm^2. The as-prepared devices were then annealed at 150 °C for 20 min in vacuum to improve the crystallinity of the P3HT:PCBM blend.

2.5. Device Characterization. The current density (J)−voltage (V) characteristics were recorded with a Keithley 2420 source meter in the dark and under illumination using a Sun 2000 solar simulator (Abet) with AM1.5 spectrum (100 mW/cm^2). The intensity of the solar simulator was determined by a standard Si photovoltaic cell calibrated by the National Renewable Energy Laboratory. Incident photon-to-electron conversion efficiency (IPCE) measurements were performed under short circuit condition with respect to a calibrated silicon diode. The IPCE was calculated using $\text{IPCE}(\lambda) = (hc/\lambda)(I(\lambda) - I_{\text{dark}})/P(\lambda)$, where $I(\lambda)$ and I_{dark} are the short circuit current recorded under illumination and in the dark, respectively. No corrections were made for reflection from the glass substrate. The
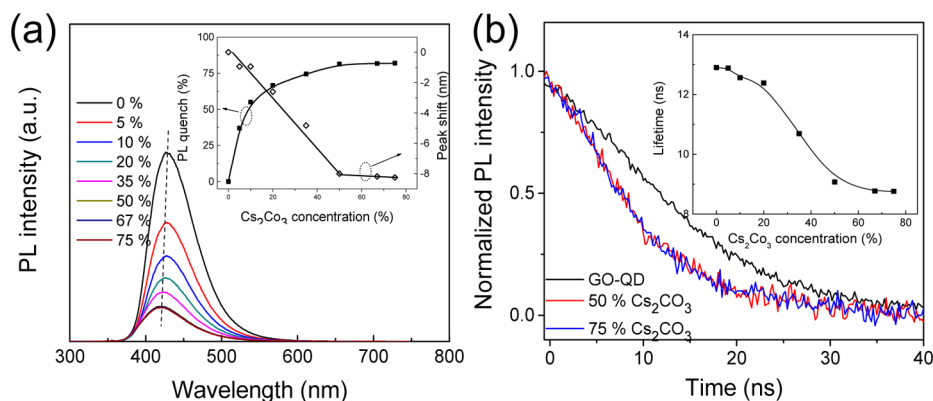
Figure 2. PL emission spectra (a) and PL emission decay (b) of GQDs−Cs₂CO₃ in ethanol with different modification concentrations of Cs₂CO₃. Insets show the relationship of PL quenching, peak shift, and lifetime of PL emission of GQDs−Cs₂CO₃ vs modification concentration of Cs₂CO₃.

monochromic light used for IPCE measurement was supplied from xenon light, which passes through a Cornerstone monochromator. A chopper was placed after the monochromator, and the signal was collected by Merlin lock-in radiometry after amplification through the current preamplifier. All measurements metioned above were performed in air at room temperature without encapsulation. During the whole degradation period of OPVs, the intensity of the decreased simulated light was neglected (less than 1%) and calibrated by a standard Si photovoltaic cell. All devices were stored in the dark under ambient environment with $60 \pm 5\%$ relative humidity at room temperature. The humidity was measured by an electric-capacity moisture meter (TH05, Wexcel).

3. RESULTS AND DISCUSSION

Figure 1a shows the TEM image of the as-prepared GQDs. The size of GQDs is quite uniform, with an average size of ∼5 nm. Raman spectroscopy was used to confirm the quality of the GQDs (Figure 1b). Two major features associated with graphene, a D band and a G band, were observed at around 1385 and 1575 cm⁻¹, respectively. The GQDs showed a broad (002) diffraction peak centered at around 26.2° (Figure 1c) in the XRD pattern, which further confirmed the layered graphene structure of the as-prepared GQDs. The topographic height obtained from AFM is in the range 0.5−2 nm (Figure 1e), suggesting that GQDs have one or two layered structure. Our results are similar to those reported for GQDs.[25−34]

Figure 2a displays the PL emission spectra of Cs₂CO₃-modified GQDs (GQDs−Cs₂CO₃). The PL intensity of GQDs−Cs₂CO₃ was decreased, and the emission peak was linearly blue-shifted with increase of Cs₂CO₃ concentration up to 50%. At a modification concentration of 50% of Cs₂CO₃, the emission of GQDs was quenched by 80%. After that, further increase in Cs₂CO₃ concentration causes little change in PL intensity and the peak position. Cs₂CO₃ modification also changed the PL emission lifetime of GQDs. As shown in Figure 2b, the PL emission lifetime of GQDs−Cs₂CO₃ was decreased from 13 to 9 ns as the concentration of Cs₂CO₃ increased from 0% to 50%. The emission and time revolved PL results suggest that during Cs₂CO₃ modification, Cs⁺ ions could be attached onto the GQDs and form a new stable fluorophor (GQDs−Cs), which would lower the PL emission yield and shorten the emission lifetime. ζ potential measurements confirmed the presence of positively charged Cs⁺ ions on GQDs (as shown in Figure S1). The Cs⁺ ions could be adsorbed on negatively charged GQDs through the formation of −COO−Cs.

The attachment of Cs on GQDs was further probed with Fourier transform infrared (FTIR) spectroscopy. The FTIR

spectrum (Figure 3a) of pristine GQDs shows the presence of oxygen-containing functional groups on the surface: −OH
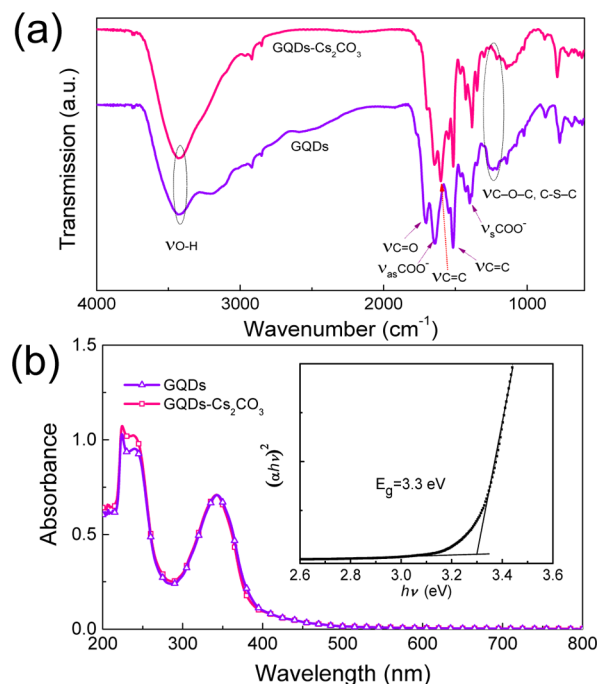

Figure 3. (a) FTIR spectra of GQDs and GQDs−Cs₂CO₃ and (b) UV−vis spectra of GQDs and GQDs−Cs₂CO₃ (1:1 in mass, 2 mg/mL GQDs). Inset of (b) is the plot of $(\alpha h\nu)^2$ vs the photon energy $h\nu$.

stretching vibration (3428 cm⁻¹), asymmetry (1643 cm⁻¹) and symmetry (1400 cm⁻¹) stretching of COOH groups, −C=O stretching vibration (1703 cm⁻¹), and −C−O−C− group (1250 cm⁻¹).[37] After modification with Cs₂CO₃, all bands related to the oxygen-containing functional groups remained in the FTIR spectrum for GQDs−Cs₂CO₃; however, the intensity of the carboxyl groups at 1643 and 1400 cm⁻¹ and the intensity of the epoxy group at 1250 cm⁻¹ were significantly reduced or disappeared, showing that the Cs had been successfully grafted on the surface of GQDs by the formation of −COO−Cs. In addition, the appearance of a sharp peak located at 1600 cm⁻¹ (aromatic C=C skeletal vibrations from unoxidized graphitic domains) on GQDs−Cs₂CO₃ could be attributed to the reduction of GQDs during the Cs grafting.

UV−vis absorption spectrum of GQDs in Figure 3b shows two typical absorption peaks centered at 240 and 343 nm, respectively, of which the former is attributed to the $\pi \rightarrow \pi^*$ transition of the aromatic sp^2 domains, while the latter is due to electron excitation from the ground states to the excited states. The incorporation of Cs_2CO_3 in GQDs did not change the absorption. On the basis of Tauc's relation $\alpha h\nu = A(h\nu - E_g)^n$,[38] where α is the absorption coefficient, $h\nu$ is the photon energy, E_g is the optical band gap, and n equals 2 or $^1/_2$ for indirect and direct allowed transition, an estimated direct optical bandgap of the as-prepared GQDs is ∼3.3 eV (inset of Figure 3b).

Figure 4 shows the surface morphologies of Cs_2CO_3 and GQDs−Cs_2CO_3 coated ITO substrate. Cs_2CO_3 did not form a
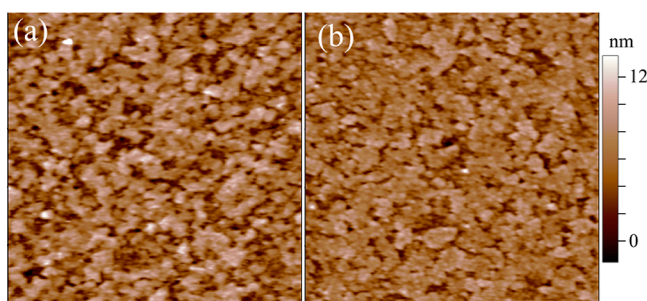
Figure 4. AFM images of (a) Cs_2CO_3 and (b) GQDs−Cs_2CO_3 on ITO substrate. The scan area is 5 × 5 μm^2.

uniform coating on ITO surface with inhomogeneous aggregates of nano-sized island. The surface roughness was estimated to be ∼2.4 nm, which is larger than that of bare ITO

surface (2.1 nm). The GQDs−Cs_2CO_3 could be more uniformly coated on ITO surface with a much smaller surface roughness of 1.8 nm. Thus, the use of GQDs−Cs_2CO_3 composite buffer in PSCs may improve the charge transport as well as the reproducibility of high performance devices.

Figure 5a and Supporting Information Figure S2 show the XPS spectra of Cs_2CO_3 and GQDs−Cs_2CO_3 modified ITO. As shown in the high-resolution Cs $3d_{5/2}$ spectra (Figure 5b), the binding energy of Cs $3d_{5/2}$ photoelectrons for GQDs−Cs_2CO_3 modified ITO was shifted toward a smaller value compared with that of Cs_2CO_3 modified ITO. The smaller photoelectron binding energy of Cs $3d_{5/2}$ in GQDs−Cs_2CO_3 implies the existence of additional positive charges surrounding the Cs atoms, which could be due to the electron transfer of the lone $6s^1$ electron from Cs^+ to the GQDs host.[39] Besides, the In 3d photoelectrons in ITO also shifted toward lower binding energies after modification with Cs_2CO_3 and GQDs−Cs_2CO_3. The trend of In 3d spectra shift reflects more electrons transferred from GQDs−Cs_2CO_3 to ITO than from Cs_2CO_3 to ITO. This electron transfer increasing the the electric dipole moment at the interface could push up the Fermi level of the ITO surface and lower its work function.[40]

The work function of Cs_2CO_3 and GQDs−Cs_2CO_3 modified ITO surface was investigated using ultraviolet photoelectron spectroscopy (UPS). The secondary cut-off region (E_{cutoff}) and E_F are defined in Figure 5d, and the work function was calculated using eq 1.

$$\phi = h\nu - E_{cut\text{-}off} + E_{Fermi} \tag{1}$$

where $h\nu$ (21.2 eV) is the incoming photon energy from the He source. As shown in Figure 5d, the work function of ITO (4.55
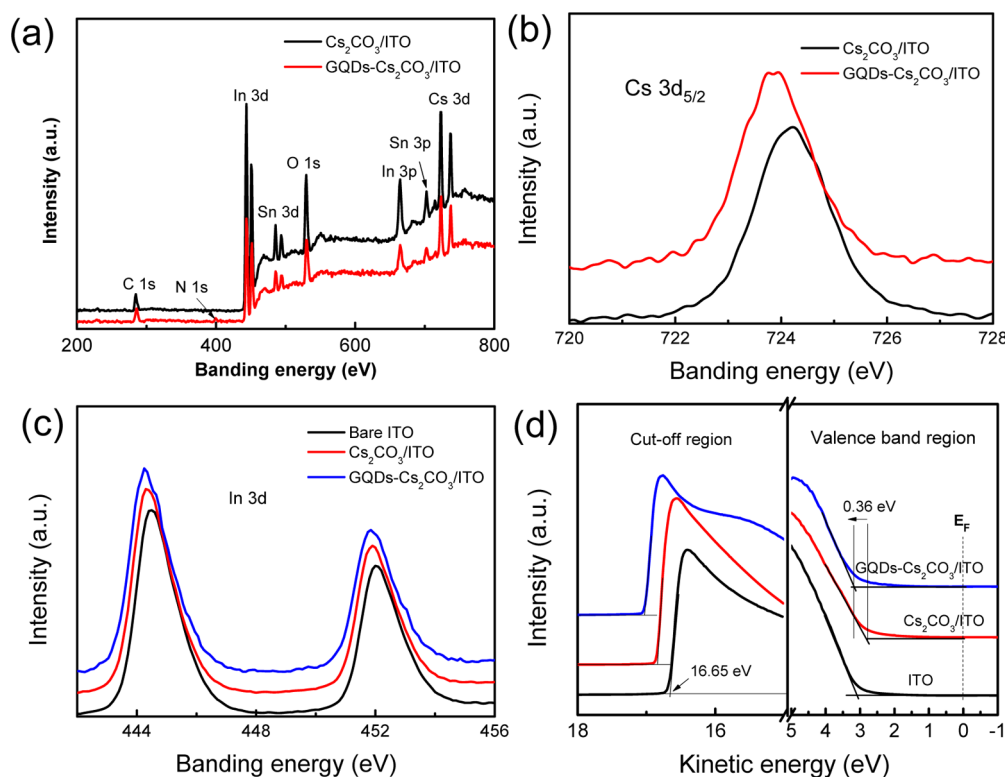
Figure 5. (a) XPS spectra of Cs_2CO_3 and GQDs−Cs_2CO_3 on ITO substrate. (b) Cs $3d_{5/2}$ and (c) In 3d XPS spectra. (d) Evolution of the secondary electron edge in UPS spectra measured for bare ITO, Cs_2CO_3 and GQDs−Cs_2CO_3 modified ITO. The left and right parts of (d) are the cut-off region and the valence band region.
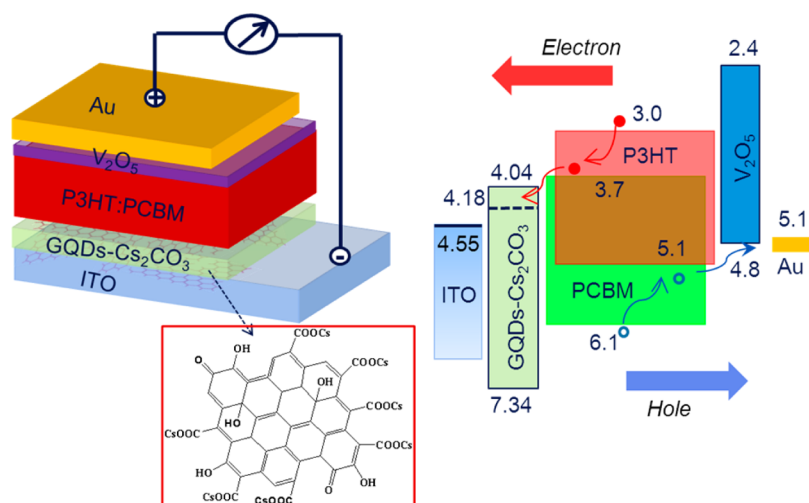
Figure 6. Schematic structure (left) and energy band diagram (right) of an inverted polymer solar cell with GQDs−Cs$_2$CO$_3$ buffer layer.
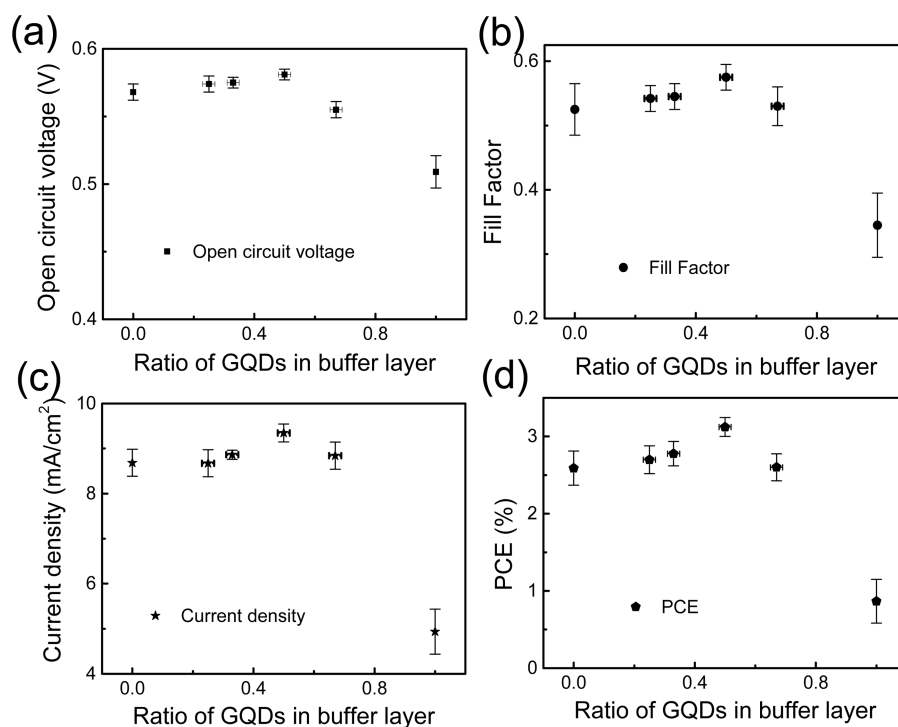

Figure 7. Photovoltaic properties of GQDs−Cs$_2$CO$_3$ buffed inverted P3HT:PCBM solar cells with different concentrations of GQDs in GQDs−Cs$_2$CO$_3$.

eV) shifted 0.19 and 0.37 eV toward the higher energy level by coating ITO with Cs$_2$CO$_3$ and GQDs−Cs$_2$CO$_3$, respectively, which agrees well with the XPS results. Compared with Cs$_2$CO$_3$ buffer, the GQDs−Cs$_2$CO$_3$ buffer has a better energy match with the lowest unoccupied molecular orbital (LUMO) of PCBM (3.7 eV). The well-matched energy level at electrode/polymer active layer interface of PSCs could minimize the energy loss at the interface during charge separation to result in higher open-circuit voltage (V_{oc}) and larger short-circuit current (J_{sc}). Valence band spectra of buffer layer modified ITO are shown in the right part of Figure 5d. The valence band maximum (VBM) of Cs$_2$CO$_3$ and GQDs−Cs$_2$CO$_3$ modified ITO are located about 2.8 and 3.16 eV below the Fermi level, suggesting that GQDs−Cs$_2$CO$_3$ buffer has better hole blocking ability in PSCs.

On the basis of the AFM, XPS, and UPS results, it can be speculated that GQDs−Cs$_2$CO$_3$ buffer would be beneficial for constructing PSCs with high power conversion efficiency (PCE). Figure 6 shows the schematic structure and energy band diagram of an inverted P3HT:PCBM solar cell with GQDs−Cs$_2$CO$_3$ electron-selective layer, in which energy level of GQDs−Cs$_2$CO$_3$ buffer was calculated based on UV−vis and UPS measurements.

To access the influence of GQDs−Cs$_2$CO$_3$ buffer on the performance of P3HT:PCBM inverted polymer solar cells, a series of devices (ITO/cathode buffer (Cs$_2$CO$_3$ or GQDs−Cs$_2$CO$_3$)/P3HT:PCBM/V$_2$O$_5$/Au) with varying ratios of GQDs to Cs$_2$CO$_3$ in GQDs−Cs$_2$CO$_3$ buffer were examined ($J−V$ curves are shown in Figure S3). Figure 7 shows the averaged device characteristics of P3HT:PCBM inverted
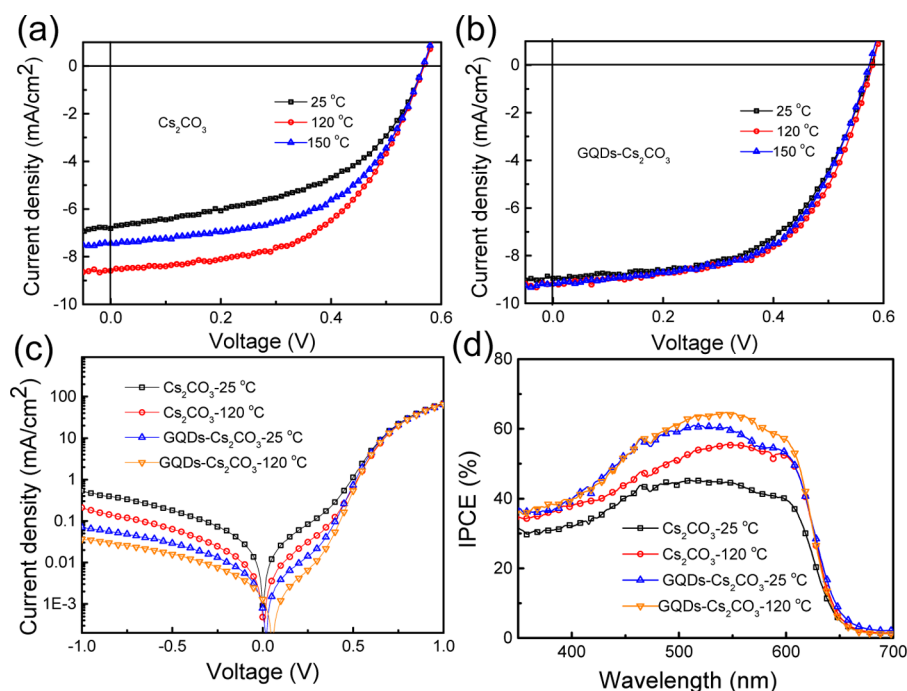
Figure 8. $J-V$ curves of inverted P3HT:PCBM devices with (a) Cs_2CO_3 and (b) $GQDs-Cs_2CO_3$ (50% of GQDs) buffer layer that are annealed at different temperatures under AM1.5 illumination and (c) in the dark. (d) IPCE spectra of the corresponding devices.

Table 1. Photovoltaic Properties of Inverted P3HT:PCBM PSCs with Cs_2CO_3 and $GQDs-Cs_2CO_3$ Buffer Thermally Annealed at 25, 120, and 150 °C[a]

| buffer	temp (°C)	PCE (%)	V_{oc} (V)	J_{sc} (mA/cm^2)	FF (%)
Cs_2CO_3	25	*1.96*	*0.569*	*6.81*	*50.6*
		1.91 (±0.05)	0.571 (±0.002)	6.62 (±0.21)	50.6 (±1.5)
	120	*2.72*	*0.574*	*8.59*	*55.2*
		2.67 (±0.07)	0.571 (±0.004)	8.51 (±0.14)	54.9 (±1.4)
	150	*2.39*	*0.572*	*7.44*	*56.0*
		2.38 (±0.05)	0.570 (±0.003)	7.46 (±0.11)	55.9 (±1.8)
$GQDs-Cs_2CO_3$	25	*3.05*	*0.583*	*8.95*	*58.5*
		2.99 (±0.06)	0.582 (±0.001)	9.04 (±0.16)	57.4 (±1.4)
	120	*3.23*	*0.585*	*9.18*	*60.1*
		3.16 (±0.05)	0.585 (±0.001)	9.14 (±0.13)	59.1 (±1.2)
	150	*3.21*	*0.580*	*9.18*	*60.4*
		3.14 (±0.09)	0.579 (±0.002)	9.17 (±0.23)	59.2 (±1.5)

[a]Data and statistics are based on two batches and in total eight cells of each buffer. Numbers in bold italic are the maximum recorded values.

polymer solar cells with Cs_2CO_3 or $GQDs-Cs_2CO_3$ buffer layer. Similar to the trend observed in PL emission and PL emission decay studies, the I_{sc}, V_{oc}, and FF of devices buffered with $GQDs-Cs_2CO_3$ was first increased with an increase in concentration of GQDs from 0% to 50% in the buffer, resulting in the improvement of PCE from 2.72% to 3.23%. Afterward, further increase in the percentage of GQDs in the buffer layer resulted in deterioration of the device performance. For inverted PSCs buffered with pure GQDs, the PCE is about 0.8%, mainly due to low photocurrent density (4.9 mA/cm^2) and poor FF (35%), which should be attributed to poor electron extraction ability of the GQDs buffer because of the insulating characteristic of strongly oxidized GQDs.

To further show the advantages of the $GQDs-Cs_2CO_3$ composite buffer, the effects of thermal treatment of Cs_2CO_3 and $GQDs-Cs_2CO_3$ (50%) on the device performance were studied in detail. Parts a and b of Figure 8 show the $J-V$ characteristics of inverted PSCs made with Cs_2CO_3 and

$GQDs-Cs_2CO_3$ buffer at various thermal treatment temperatures. The performance parameters are summarized in Table 1. When Cs_2CO_3 buffered inverted PSCs were treated at elevated temperatures, all devices showed improved performance. The device performance depends on the thermal treatment temperature. The I_{sc} and FF increased from 6.81 mA/cm^2 and 50.1% to 8.59 mA/cm^2 and 56%, respectively, resulting in the improvement of PCE from 1.96% to 2.72% as the thermal treatment temperature increased from room temperature to 120 °C, which is comparable to the reported results for Cs_2CO_3 buffered devices.[9,23,24] A further increase in the annealing temperature led to poorer device performance, which can be attributed to reduced work function and interface resistance of the buffer layer under high temperature thermal treatment.[9] However, in the case of $GQDs-Cs_2CO_3$ buffered devices, the $J-V$ curves almost did not change before and after the thermal treatment. In addition, the devices are more stable under high temperature thermal treatment compared with

1097

dx.doi.org/10.1021/am404638e | ACS Appl. Mater. Interfaces 2014, 6, 1092−1099
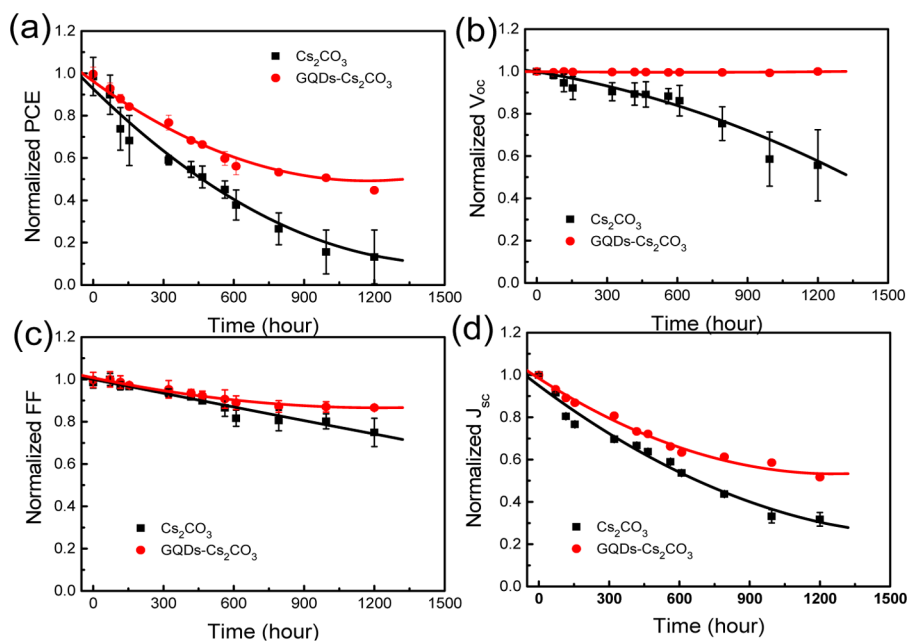
Figure 9. Changes of solar cell parameters of P3HT:PCBM inverted solar cells with Cs_2CO_3 and $GQDs-Cs_2CO_3$ buffer in ambient air condition with 65% relative humidity.

Cs_2CO_3 buffered devices. The current−voltage characteristics of devices with Cs_2CO_3 and $GQDs-Cs_2CO_3$ buffer in the dark (Figure 8c) show typical diode behaviors. In comparison with the as-fabricated devices without thermal treatment, the devices annealed at 120 °C have smaller leakage current, which indicates that buffer layer annealing could increase the device shunt resistance, thus improving the hole blocking ability of the buffer and enhancing the device performance. It can be seen that the reverse leakage current for $GQDs-Cs_2CO_3$ buffered devices is always lower than that of Cs_2CO_3 buffered devices, independent of the thermal treatment temperature. Moreover, the leakage current of 120 °C treated device buffered with Cs_2CO_3 is more than 3 times larger than that of the $GQDs-Cs_2CO_3$ buffered device even without any thermal treatment (0.22 vs 0.07 mA/cm^2 at −1.0 V), indicating the better hole blocking ability of $GQDs-Cs_2CO_3$. The IPCE spectra of devices with Cs_2CO_3 and $GQDs-Cs_2CO_3$ buffer treated at room temperature and 120 °C are shown in Figure 8d, which agree well with the photocurrent obtained from Figure 8a and Figure 8b.

From the above studies, it can be seen that $GQDs-Cs_2CO_3$ can work as an excellent electron-selective buffer for high performance inverted PSCs, which not only has the appropriate work function and valence band for better electron extraction and hole blocking but also can sustain wider ranges of annealing temperatures without damaging the device performance. With these benefits, $GQDs-Cs_2CO_3$ should offer great process compatibility for the fabrication of solution-processable complicated PSCs, e.g., tandem structured devices.

The stability of $GQDs-Cs_2CO_3$ also shows a merit in improving the device stability. The degradation of inverted PSCs in air at room temperature and 60% relative humidity was studied, and the results are shown in Figure 9 (J−V curves are shown in Figure S4). All device characterizations were performed in air at room temperature without encapsulation. After 450 h of continuous exposure to air and moisture, the PCE of devices with the $GQDs-Cs_2CO_3$ buffer remained 70% of its original value, which is about 2 times better than that of

the Cs_2CO_3 buffered devices. The degradation of J_{sc} is similar for both devices buffered with Cs_2CO_3 and $GQDs-Cs_2CO_3$ because of the degradation of organic active layer induced by water penetration.[41−43] Apart from photocurrent degradation, the V_{oc} of devices with Cs_2CO_3 buffer shows rapid decrease over time, which is similar to the previous studies monitored in the oxygen and water free environment, due to the Cs^+ ion diffusion at the buffer/polymer interface,[29,44] while the V_{OC} of devices with $GQDs-Cs_2CO_3$ buffer maintains 99.4% of its initial value after 1200 h exposure in air at room temperature and 60% relative humidity, demonstrating the stability of $GQDs-Cs_2CO_3$ due to the immobilization of Cs on GQDs.

4. CONCLUSIONS

In summary, we have demonstrated the application of Cs_2CO_3 modified graphene quantum dots ($GQDs-Cs_2CO_3$) as a stable electron-selective buffer in improving the performance of inverted PSCs. The $GQDs-Cs_2CO_3$ exhibits excellent hole blocking and electron transfer capability due to the well-matched energy levels between $GQDs-Cs_2CO_3$ and PCBM, which improves the PCE of inverted PSCs by 56% compared with that of single Cs_2CO_3 buffered cells. The immobilization of Cs^+ ions on GQDs in $GQDs-Cs_2CO_3$ buffer further retards the Cs^+ ion diffusion into the polymer layer and thus improves the device stability. Our results suggest that $GQDs-Cs_2CO_3$ fabricated by a solution process could be beneficial for the construction of high performance all-solution-processed or roll-to-roll processed PSCs and other organic electronic devices. This work also provides an understanding toward the application of GQDs in organic electronic devices.

■ ASSOCIATED CONTENT

⑤ Supporting Information

ζ potential (Figure S1), XPS spectra of N 1s of Cs_2CO_3 and $GQDs-Cs_2CO_3$ (Figure S2), and I−V curves of inverted P3HT:PCBM PSCs with different electron-selective layer (Figure S3) and measured after different durations of

continuous exposure to air and moisture (Figure S4). This material is available free of charge via the Internet at http://pubs.acs.org.

■ AUTHOR INFORMATION

Corresponding Author
*E-mail: LiuBin@ntu.edu.sg. Phone: (+65) 6513 7971.

Notes
The authors declare no competing financial interest.

■ ACKNOWLEDGMENTS

■ REFERENCES

(1) Li, G.; Shrotriya, V.; Huang, J.; Yao, Y.; Moriarty, T.; Emery, K.; Yang, Y. *Nat. Mater.* **2005**, *4* (11), 864−868.

(2) Chen, H.-Y.; Hou, J.; Zhang, S.; Liang, Y.; Yang, G.; Yang, Y.; Yu, L.; Wu, Y.; Li, G. *Nat. Photonics* **2009**, *3* (11), 649−653.

(3) Sariciftci, N. S.; Smilowitz, L.; Heeger, A. J.; Wudl, F. *Science* **1992**, *258* (5087), 1474−1476.

(4) Krebs, F. C. *Sol. Energy Mater. Sol. Cells* **2009**, *93* (4), 394−412.

(5) Krebs, F. C.; Jørgensen, M.; Norrman, K.; Hagemann, O.; Alstrup, J.; Nielsen, T. D.; Fyenbo, J.; Larsen, K.; Kristensen, J. *Sol. Energy Mater. Sol. Cells* **2009**, *93* (4), 422−441.

(6) Amb, C. M.; Craig, M. R.; Koldemir, U.; Subbiah, J.; Choudhury, K. R.; Gevorgyan, S. A.; Jørgensen, M.; Krebs, F. C.; So, F.; Reynolds, J. R. *ACS Appl. Mater. Interfaces* **2012**, *4* (3), 1847−1853.

(7) Kim, C. S.; Lee, S. S.; Gomez, E. D.; Kim, J. B.; Loo, Y.-L. *Appl. Phys. Lett.* **2009**, *94* (11), 113302.

(8) You, J.; Chen, C. C.; Dou, L.; Murase, S.; Duan, H. S.; Hawks, S. A.; Xu, T.; Son, H. J.; Yu, L.; Li, G.; Yang, Y. *Adv Mater.* **2012**, *24* (38), 5267−5272.

(9) Liao, H.-H.; Chen, L.-M.; Xu, Z.; Li, G.; Yang, Y. *Appl. Phys. Lett.* **2008**, *92* (17), 173303.

(10) Liu, J.; Shao, S.; Fang, G.; Meng, B.; Xie, Z.; Wang, L. *Adv Mater.* **2012**, *24* (20), 2774−2779.

(11) Yang, L.; Xu, H.; Tian, H.; Yin, S.; Zhang, F. *Sol. Energy Mater. Sol. Cells* **2010**, *94* (10), 1831−1834.

(12) Yang, H.; Song, Q.; Lu, Z.; Guo, C.; Gong, C.; Hu, W.; Li, C. M. *Energy Environ. Sci.* **2010**, *3* (10), 1580−1586.

(13) Yang, H.; Gong, C.; Guai, G. H.; Li, C. M. *Sol. Energy Mater. Sol. Cells* **2012**, *101* (0), 256−261.

(14) Canesi, E. V.; Binda, M.; Abate, A.; Guarnera, S.; Moretti, L.; D'Innocenzo, V.; Kumar, R. S. S.; Bertarelli, C.; Abrusci, A.; Snaith, H.; Calloni, A.; Brambilla, A.; Ciccacci, F.; Aghion, S.; Moia, F.; Ferragut, R.; Melis, C.; Malloci, G.; Mattoni, A.; Lanzani, G.; Petrozza, A. *Energy Environ. Sci.* **2012**, *5* (10), 9068−9076.

(15) Chen, L.-M.; Xu, Z.; Hong, Z.; Yang, Y. *J. Am. Chem. Soc.* **2010**, *20* (13), 2575.

(16) Liu, J.; Xue, Y.; Gao, Y.; Yu, D.; Durstock, M.; Dai, L. *Adv Mater.* **2012**, *24* (17), 2228−2233.

(17) Sun, Y.; Seo, J. H.; Takacs, C. J.; Seifter, J.; Heeger, A. J. *Adv Mater.* **2011**, *23* (14), 1679−1683.

(18) Stubhan, T.; Salinas, M.; Ebel, A.; Krebs, F. C.; Hirsch, A.; Halik, M.; Brabec, C. J. *Adv. Eng. Mater.* **2012**, *2* (5), 532−535.

(19) Lin, Z.; Jiang, C.; Zhu, C.; Zhang, J. *ACS Appl. Mater. Interfaces* **2013**, *5* (3), 713−718.

(20) Trost, S.; Zilberberg, K.; Behrendt, A.; Polywka, A.; Görrn, P.; Reckers, P.; Maibach, J.; Mayer, T.; Riedl, T. *Adv. Eng. Mater.* **2013**, *3*, 1437−1444.

(21) Xu, Z.; Chen, L.-M.; Yang, G.; Huang, C.-H.; Hou, J.; Wu, Y.; Li, G.; Hsu, C.-S.; Yang, Y. *Adv. Funct. Mater.* **2009**, *19* (8), 1227−1234.

(22) Lee, Y.-I.; Youn, J.-H.; Ryu, M.-S.; Kim, J.; Moon, H.-T.; Jang, J. *Sol. Energy Mater. Sol. Cells* **2011**, *95* (12), 3276−3280.

(23) Cheng, G.; Tong, W.-Y.; Low, K.-H.; Che, C.-M. *Sol. Energy Mater. Sol. Cells* **2012**, *103*, 164−170.

(24) Lee, Y.-I.; Youn, J.-H.; Ryu, M.-S.; Kim, J.; Jang, J. *Org. Electron.* **2012**, *13* (8), 1302−1307.

(25) Dong, Y.; Pang, H.; Yang, H. B.; Guo, C.; Shao, J.; Chi, Y.; Li, C. M.; Yu, T. *Angew. Chem., Int. Ed.* **2013**, *52* (30), 7800−7804.

(26) Chen, L.; Guo, C. X.; Zhang, Q.; Lei, Y.; Xie, J.; Ee, S.; Guai, G.; Song, Q.; Li, C. M. *ACS Appl. Mater. Interfaces* **2013**, *5* (6), 2047−2052.

(27) Dong, Y.; Chen, C.; Zheng, X.; Gao, L.; Cui, Z.; Yang, H.; Guo, C.; Chi, Y.; Li, C. M. *J. Mater. Chem.* **2012**, *22* (18), 8764−8766.

(28) Li, H.; He, X.; Kang, Z.; Huang, H.; Liu, Y.; Liu, J.; Lian, S.; Tsang, C. H. A.; Yang, X.; Lee, S.-T. *Angew. Chem., Int. Ed.* **2010**, *49* (26), 4430−4434.

(29) Son, D. I.; Kwon, B. W.; Park, D. H.; Seo, W.-S.; Yi, Y.; Angadi, B.; Lee, C.-L.; Choi, W. K. *Nat. Nanotechnol.* **2012**, *7* (7), 465−471.

(30) Wang, F.; Chen, Y.-h.; Liu, C.-y.; Ma, D.-g. *Chem. Commun.* **2011**, *47* (12), 3502−3504.

(31) Guo, C. X.; Dong, Y.; Yang, H. B.; Li, C. M. *Adv. Eng. Mater.* **2013**, *3* (8), 997−1003.

(32) Li, Y.; Hu, Y.; Zhao, Y.; Shi, G.; Deng, L.; Hou, Y.; Qu, L. *Adv. Mater.* **2011**, *23* (6), 776−780.

(33) Gupta, V.; Chaudhary, N.; Srivastava, R.; Sharma, G. D.; Bhardwaj, R.; Chand, S. *J. Am. Chem. Soc.* **2011**, *133* (26), 9960−9963.

(34) Mirtchev, P.; Henderson, E. J.; Soheilnia, N.; Yip, C. M.; Ozin, G. A. *J. Mater. Chem.* **2012**, *22* (4), 1265.

(35) Nurunnabi, M.; Khatun, Z.; Nafiujjaman, M.; Lee, D.-g.; Lee, Y.-k. *ACS Appl. Mater. Interfaces* **2013**, *5* (16), 8246−8253.

(36) Xue, Y.; Liu, Y.; Lu, F.; Qu, J.; Chen, H.; Dai, L. *J. Phys. Chem. Lett.* **2012**, *3* (12), 1607−1612.

(37) Wang, D.-W.; Wu, K.-H.; Gentle, I. R.; Lu, G. Q. *Carbon* **2012**, *50* (9), 3333−3341.

(38) Tauc, J. *Amorphous and Liquid Semiconductors*; Plenum: New York, 1974.

(39) Luo, X.; Fang, C.; Li, X.; Lai, W.; Liang, T. *J. Nucl. Mater.* **2013**, *441* (1−3), 113−118.

(40) Batzill, M.; Diebold, U. *Prog. Surf. Sci.* **2005**, *79* (2−4), 47−154.

(41) Lee, J. U.; Jung, J. W.; Jo, J. W.; Jo, W. H. *J. Am. Chem. Soc.* **2012**, *22* (46), 24265.

(42) Nikiforov, M. P.; Strzalka, J.; Darling, S. B. *Sol. Energy Mater. Sol. Cells* **2013**, *110*, 36−42.

(43) Yang, H. B.; Song, Q. L.; Gong, C.; Li, C. M. *Sol. Energy Mater. Sol. Cells* **2010**, *94* (5), 846−849.

(44) Lee, Y.-I.; Youn, J.-H.; Ryu, M.-S.; Kim, J.; Moon, H.-T.; Jang, J. *Org. Electron.* **2011**, *12* (2), 353−357.